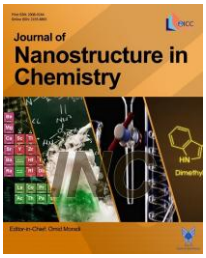

J. Nanostruct Chem. 2026; 16(4): 319-331

Journal of Nanostructure in Chemistry (JNSC)

https://doi.org/10.57647/jnsc.2026.1604.16

Research Article

# A Machine Learning-assisted Smartphone-based Method for Rapid Quantification of Total Flavonoids by Quantum Dots

Ying Chen[1,#], Yiyu Qi[1,#], Ao Qian[1], Jie Li[1], Jiaqi Guo[2], Yuchen He[1], Hassan Algadi[3], Juanna Ren[4], Bingnan Yuan[1,*], Zhanhu Guo[5,*], Yi Kuang[1,*]

[1] *College of Chemistry and Materials Engineering, Zhejiang A&F University, Hangzhou 311300, PR China*
[2] *Health Science Center, Ningbo University, Ningbo 315211, Zhejiang, PR China*
[3] *Department of Electrical Engineering, Faculty of Engineering, Najran University, Najran, 11001, Saudi Arabia*
[4] *College of Materials Science & Engineering, Taiyuan University of Science & Technology, Taiyuan 030024, PR China*
[5] *Department of Mechanical and Construction Engineering, Northumbria University, Newcastle, Upon Tyne, NE1 8ST, UK*

[#] *Ying Chen and Yiyu Qi equally contributed to this work.*

[*] **Corresponding authors:** ybn@zafu.edu.cn, zhanhu.guo@northumbria.ac.uk, kuangyi@zafu.edu.cn

**Article History:**

Received:
19 October 2025

Revised:
31 January 2026

Accepted:
05 April 2026

Published in Issue:
31 August 2026



**Abstract**

This study presents a rapid and instrument-free method for the quantification of total flavonoids, utilizing smartphone imaging and lightweight machine learning techniques. The methodology involves capturing fluorescence images of zinc-based quantum dots that are quenched by varying concentrations of quercetin, a representative flavonoid, using a smartphone camera. A pre-trained convolutional neural network (CNN) model was developed, which can be fine-tuned with a minimal dataset to achieve accurate quantification of total flavonoids in specific plant samples. Using *Euphorbia humifusa* as a model plant, the method demonstrated a linear detection range of 5–500 μg/mL, with quantification errors ranging from 0.1 to 10 μg/mL. Compared to conventional methods, the detection limit was improved by a factor of 1.6, and the upper detection limit was also extended by a factor of 1.6. This approach provides simplicity, cost-effectiveness, and independence from specialized instruments, thereby offering a promising solution for on-site rapid detection of total flavonoids in plants.

**Keywords:** Convolutional neural network; Machine learning; Quantum dots; Rapid quantification; Smartphone-based detection

**Cite this article:** Chen Y., Qi Y., Qian A., Li J., Guo J., He Y., Algadi H., Ren J., Yuan B., Guo Zh., Kuang Y. A machine learning-assisted smartphone-based method for rapid quantification of total flavonoids by quantum dots. *J Nanostruct Chem* 16, 319-331 (2026). https://doi.org/10.57647/jnsc.2026.1604.16

## 1. Introduction

Flavonoids represent a significant class of natural products that are widely distributed across the plant kingdom, exhibiting notable antioxidant and anti-inflammatory properties [1-3]. These compounds play crucial roles in protecting the cardiovascular, nervous, and immune systems, regulating metabolism, inhibiting tumor growth, and maintaining intestinal health. As essential "phytochemical guardians", flavonoids are vital for human health and the prevention of chronic diseases. The realization of their remarkable medicinal value is contingent upon the quality of the source plants or herbal materials, making the quality assessment of these sources critically important [4-5]. Quantitative detection of total flavonoids in plant extracts constitutes a crucial step in quality evaluation. Currently, ultraviolet-visible spectrophotometry serves as the gold standard for total flavonoid quantification; however, it suffers from limitations, including a narrow linear range and heavy

instrument dependence. Quantum dots (QDs) have emerged as key tools in modern quantitative analysis due to their exceptional optical properties [6-7]. The interaction between target analytes and QDs results in fluorescence quenching or enhancement, which can be quantitatively assessed to determine analyte concentration [8]. Sulfur-doped graphene quantum dots (SGQDs) serve as sensitive fluorescent probes for quercetin detection in red wine. SGQDs exhibit significant fluorescence quenching when interacting with quercetin, providing a low-cost and efficient method for real-time quantitation [9]. Similarly, carbon dots (CDs) derived from olive tree pruning residues serve as a highly selective fluorescent probe that can specifically detect trivalent iron ions ($Fe^{3+}$) through significant fluorescence quenching effects, providing a green and sensitive analytical method for identifying iron species in water and food samples [10]. Furthermore, polyethylene glycol-400-capped sulfur quantum dots (PEG SQDs) have been employed to achieve highly sensitive and selective detection of quercetin (QT) through static quenching and internal filtration effects, and have been successfully applied to the analysis of actual samples such as human serum, health products, and red wine, as well as to cell imaging. However, analyzing QD fluorescence signals still requires specialized instruments and complex software, which limits most quantum dot–based detection methods to laboratory environments. Although recent studies have demonstrated the use of sulfur-doped graphene quantum dots, carbon dots from olive pruning residues, and PEG-capped sulfur quantum dots for sensitive fluorescence detection of quercetin or metal ions, their practical application remains dependent on conventional spectroscopic analysis. Our research group has explored the use of smartphone-captured images to rapidly analyze the fluorescence response of quantum dots for concentration determination, which could significantly accelerate the detection process. Nevertheless, due to the nonlinear relationship between image data and actual concentrations, achieving accurate quantification without specialized instruments remains challenging. Recent advances in machine learning provide promising solutions to address this limitation. In the field of predicting the optical properties of quantum dots, machine learning has shown great potential [11]. For example, Ed Dahmouny et al. [12] compared multiple algorithms and found that the random forest regressor can accurately predict the electric-field-dependent light absorption coefficient of CdTe/CdS core-shell quantum dots in different media. Similarly, Cherni et al. [13] successfully achieved high-precision prediction of the temperature dependent nonlinear optical rectification coefficient of GaAs/AlGaAs four-legged quantum dots by combining finite element and machine learning methods, further verifying the effectiveness and applicability of machine learning in the design of quantum dot optoelectronic devices. Besides the above machine learning algorithms, artificial neural networks (ANNs) represent the most widely applied approach in the food and pharmaceutical industries. However, traditional ANNs suffer from poor interpretability, tendencies to overfit, and requirements for large training datasets, which limit their application in image-based concentration detection [14-17]. Recent developments in neural network technology have given rise to more sophisticated architectures, such as convolutional neural networks (CNNs) and Transformers, which demonstrate excellent autonomous learning capabilities for specific data types [18-20]. In particular, CNNs exhibit outstanding performance in image analysis and modeling. These advantages have facilitated their widespread application in food safety monitoring, environmental sensing, and clinical diagnostics [21-24]. Nevertheless, building CNNs models requires substantial training datasets and is typically constrained to specific tasks. In deep learning, models pre-trained on readily available large-scale datasets can acquire general features that provide a foundation for subsequent specific tasks. These pre-trained models can then be fine-tuned using smaller task-specific training sets to achieve adaptability to target tasks with reduced data requirements.

This study proposes an innovative approach that integrates QDs, smartphone imaging, CNNs, and pre-training-fine-tuning for the rapid and intelligent detection of total flavonoid concentrations. The method exploits the concentration-dependent fluorescence quenching characteristics observed during interactions between representative flavonoid components (e.g., quercetin) and QDs. Images of quenched fluorescence captured by smartphones are processed using a pre-trained CNNs model, which is subsequently fine-tuned with crude extracts from test plants to ascertain total flavonoid content. Experimental validation was performed by measuring the total flavonoid content in *Euphorbia humifusa*. Compared to other QD-based detection methods, this approach is faster and facilitates instrument-free detection. In relation to other machine learning methods, it fully utilizes the capabilities of CNNs in image analysis while significantly reducing the requirements for training datasets through pre-training-fine-tuning, thereby achieving superior detection range and accuracy. This work represents a significant innovation in the field of intelligent portable chemical analysis technology, offering novel research directions for technological advancement in this domain.

## 2. Experiment section

### 2.1. Materials

Zinc chloride ($ZnCl_2$, 98%, Energy chemical, China),

10.57647/jnsc.2026.1604.16

Sodium citrate (98%, Energy chemical, China), Methanol ($CH_3OH$, 99.9%, Energy chemical, China), Quercetin (97%, Energy chemical, China), Lithium chloride (LiCl, 99%, Energy chemical, China), Magnesium chloride (anhydrous) ($MgCl_2$, 99%, Energy chemical, China), Aluminium chloride ($AlCl_3$, 99%, Energy chemical, China), Cadmium chloride hemi (pentahydrate) ($CdCl_2 \cdot 2.5H_2O$, 99%, Energy chemical, China), Cobalt chloride (anhydrous) ($CoCl_2$, 99%, Energy chemical, China), Chromic chloride (hexahydrate) (98%, Energy chemical, China), Copper chloride (dihydrate) (99%, Energy chemical, China), Potassium chloride (KCl, 99.5%, Energy chemical, China), Manganese chloride ($MnCl_2$, 99%, Energy chemical, China), Sodium chloride (NaCl, 99.9%, Energy chemical, China), Nickel chloride ($NiCl_2$, 98%, Energy chemical, China), iPhone 14, Huawei P30, Fluorescent lamp (SPN-VIN365, Spectroline, USA ), Transmission electron microscope (FEI Tecnai F20, USA), FTIR spectroscopy (Nicolet 6700, Thermo Scientific, USA), UV-Vis spectrophotometer (UV-2550, Shimadzu, Japan), Deionized water (prepared in-house), X-ray diffraction (XRD, Malvern Panalytical X'Pert3 Powder, Netherlands), X-ray photoelectron spectroscopy (XPS, Thermo Scientific K-Alpha, USA), Steady-State/Transient Fluorescence Spectrometer (FLS1000, Edinburgh Instruments, UK).

### 2.2. Preparation of QDs

A one-step hydrothermal synthesis of CDs was performed by dispersing 0.108 mmol of $ZnCl_2$ and 0.033 mmol of sodium citrate into 30.0 mL of deionized water (pH = 8.5). After the mixture was sonicatedto achieve complete dissolution, it was transferred to a 100 mL stainless steel autoclave lined with polytetrafluoroethylene (PTFE). The autoclave containing the reaction components was heated in a vacuum oven at 180 °C for 12 hours to synthesize CDs. Once the reaction vessel cooled down, the reaction mixture was filtered through a 0.22 μm filter. The resulting CD solution was then freeze-dried under vacuum at -40 ℃ for 48 hours and stored for future use.

### 2.3. Investigation of Quantum Dot Properties

QDs (2 g) were dispersed in 60 mL deionized water to prepare an aqueous quantum dot solution, which was stored for subsequent use. This study involves recording the emission wavelengths at excitation wavelengths of 330, 340, 350, 360, and 370 nm. Additionally, the peak fluorescence intensity of QDs will be documented at pH values of 1, 3, 5, 7, 9, and 11. A comparative analysis of the peak fluorescence intensity across five different batches of QDs will also be conducted. Furthermore, the peak fluorescence intensity will be measured after storage periods of 0, 15, 30, and 45 days. The impact of UV light (365nm, 1.2 mW/cm²) exposure on the peak fluorescence intensity of QDs will be assessed at intervals of 1, 30, 60, and 120 minutes. Similarly, the effects of direct sunlight exposure on the peak fluorescence intensity will be measured at the same time intervals. Moreover, the variations in peak fluorescence intensity of QDs will be examined under interference from various ions, including $Li^+$, $Mg^{2+}$, $Al^{3+}$, $Cd^{2+}$, $Co^{2+}$, $Cr^{3+}$, $Cu^{2+}$, $K^+$, $Mn^{2+}$, $Na^+$, $Ni^{2+}$, $Zn^{2+}$, and anions such as $HCO_3^-$, $Cl^-$, $OH^-$, $SO_4^{2-}$, $ClO^-$, and $ClO_2^-$. Lastly, the effects of typical interferents commonly found in plant extracts, such as phenolic acids, alkaloids, polysaccharides, and reducing substances, were investigated. Representative components including chlorogenic acid (CGA), berberine hydrochloride (BBR), starch, carboxylated cellulose nanocrystals (CNC), and vitamin C (VC) were selected.

### 2.4. Characterizations of QDs

The synthesized QDs were systematically characterized by transmission electron microscopy (TEM), photoluminescence spectroscopy (PL), Fourier transform infrared spectroscopy (FTIR), and ultraviolet-visible absorption spectroscopy (UV-Vis).

### 2.5. Detection of Quercetin

The flowchart for the detection of quercetin is shown in Fig. 1. The QD reserve solution described in Section 2.3 was used. Solutions with different concentrations (0-500 μg/mL) of quercetin were prepared and 250 μL of each solution was mixed with 1.95 mL of quantum dot solution in glass vials. Then, the vial was placed into the camera box (Fig. S1), which was kept in a dark environment and illuminated with a 365 nm UV lamp. The sample was placed 10 cm in front of the light source, and the smartphone was positioned parallel to the light source at a 30° angle to the sample. Images were taken using the smartphone camera against a black background. During the image capture of all samples, the relative positions of the sample, light source, and smartphone, as well as the dark ambient conditions, were kept constant. The RGB channel matrix of the captured images was input into machine learning models to determine the concentration of quercetin. The machine learning models (including CNN and ANN) were developed using Python.

### 2.6. Determination of Total Flavonoids in *E. humifusa*

Reflux-extract 0.5 g dried *E. humifusa* with 30 mL of 50% (v/v) methanol for 2 h. Repeat the procedure twice, pool the extracts, and concentrate by rotary evaporation. Reconstitute the concentrate to 30 mL with 50% (v/v) methanol. Prepare different concentrations of *E. humifusa*

10.57647/jnsc.2026.1604.16

extract according to the method for determining total flavonoids (Fig. S2).

Quercetin, as one of the components of total flavonoids in *E. humifusa*, is an important indicator for content determination. Therefore, the model established in Section 2.5 for the quantitative determination of quercetin will be used as a pre-training model and fine-tuned for measuring total flavonoids in *E. humifusa* (Fig. 1).

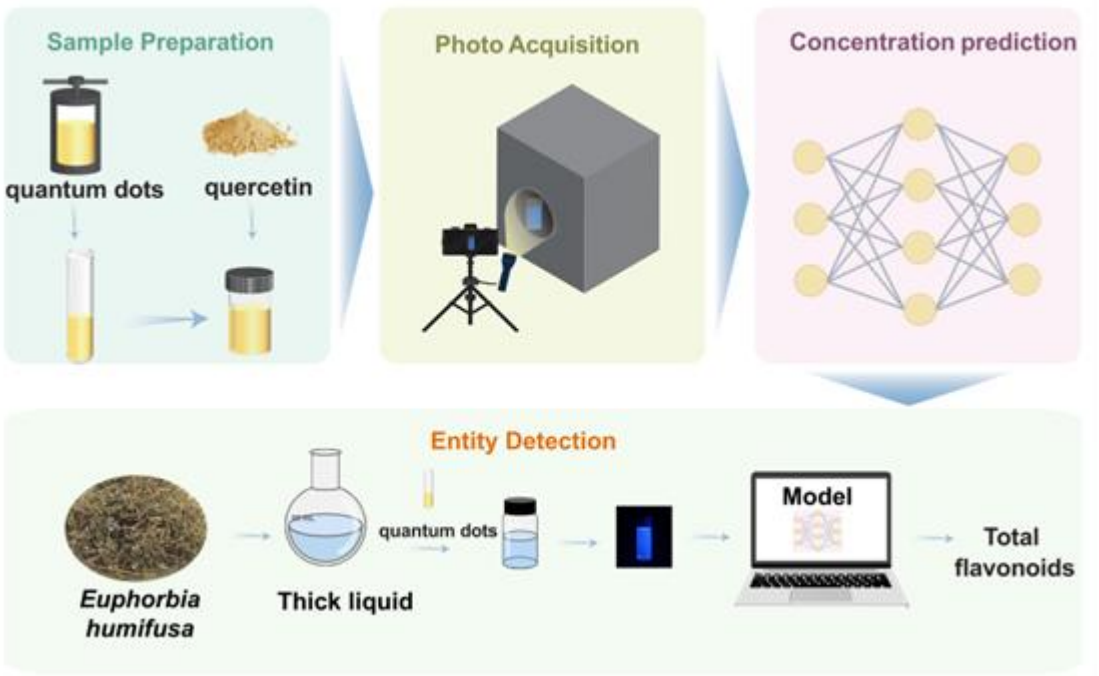


**Figure 1.** Flowchart of smartphone-based rapid fluorescence quantification methodology for total flavonoids in *Euphorbia humifusa* using Zn-based QDs with machine learning

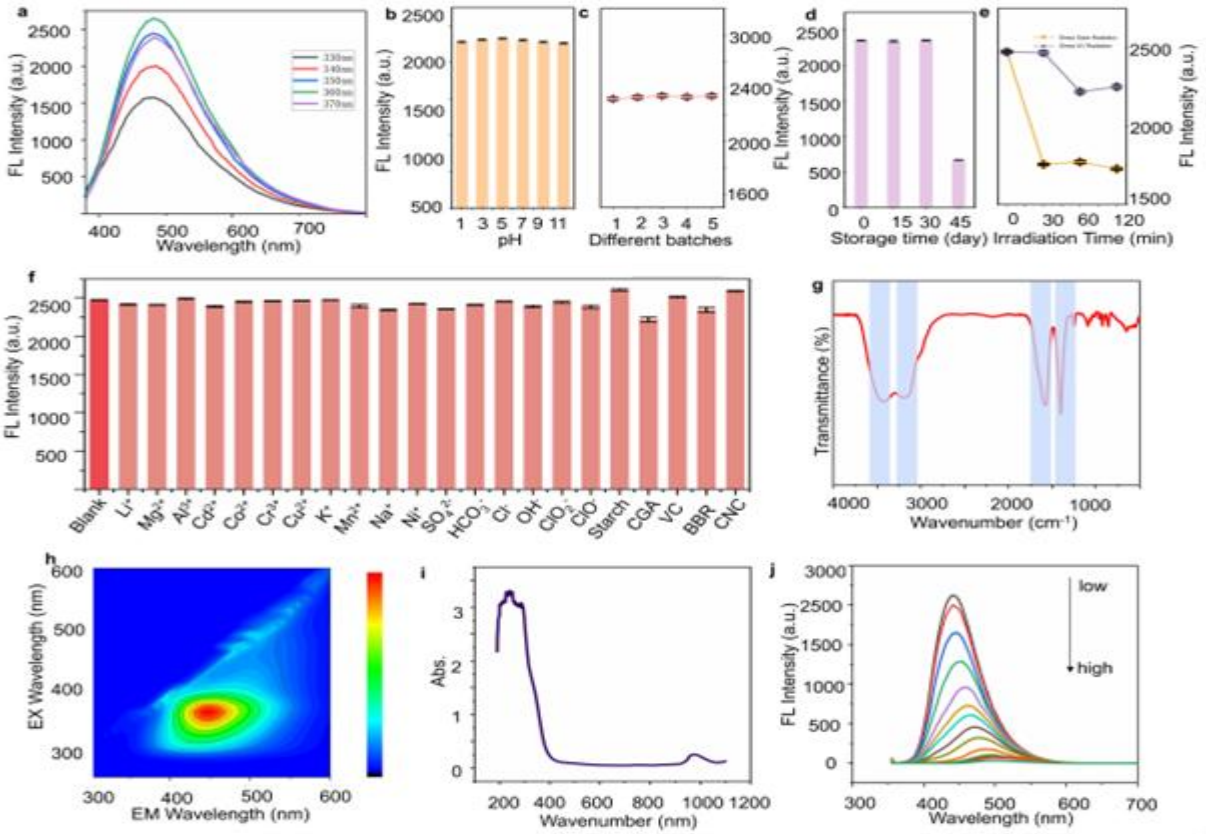


**Figure 2.** fluorescence properties, Structural and optical characterization of zinc-based QDs. (a) Excitation wavelength-dependent fluorescence intensity. (b) pH-dependent fluorescence intensity. (c) Batch-to-batch fluorescence variability. (d) Storage time-dependent fluorescence stability. (e) Photostability under UV/sunlight irradiation. (f) The influence of ion and organic interference on fluorescence intensity. (g) FTIR spectrum. (h) Emission spectrum. (i) UV-vis absorption spectrum of QDs. (j) Concentration-dependent fluorescence quenching by quercetin

10.57647/jnsc.2026.1604.16

## 3. Results and Discussion

### 3.1. Investigation of Quantum Dot Properties

At excitation wavelengths of 330, 340, 350, 360, and 370 nm, the emission wavelength of the QDs remains fixed at 450 nm, with the maximum fluorescence intensity observed at an excitation wavelength of 360 nm (Fig. 2a). Consequently, the optimal excitation wavelength for the QDs is established as 360 nm, corresponding to an emission wavelength of 450 nm. The maximum absorption intensity of quantum dot fluorescence exhibits minimal variation across pH values of 1, 3, 5, 7, 9, and 11 (Fig. 2b), indicating that the QDs demonstrate robust acid-base stability. Among the five batches analyzed, the maximum absorption intensity of quantum dot fluorescence remains consistent (Fig. 2c), suggesting stable synthesis conditions with negligible differences in the produced QDs. The quantum dot solution exhibits minimal change after 30 days of storage; however, after 45 days, there is a marked decrease in fluorescence intensity (Fig. 2d). Therefore, it is recommended that liquid QDs be utilized within 30 days, and for long-term storage, freeze-drying is advised. Under UV irradiation, the fluorescence intensity of the QDs shows minor fluctuations within the first 30 minutes, but experiences a slight decline after 60 minutes (Fig. 2e), indicating some resistance to UV exposure. Conversely, after 30 minutes of direct sunlight exposure, the fluorescence intensity of the QDs significantly diminishes (Fig. 2e). Thus, it is imperative to avoid direct sunlight exposure during the use and storage of QDs. Under the influence of $Li^+$、$Mg^{2+}$、$Al^{3+}$、$Cd^{2+}$、$Co^{2+}$、$Cr^{3+}$、$Cu^{2+}$、$K^+$、$Mn^{2+}$、$Na^+$、$Ni^{2+}$、$HCO_3^-$、$Cl^-$、$OH^-$、$SO_4^{2-}$、$ClO^-$ and $ClO_2^-$, the maximum absorption intensity of fluorescence remains largely unchanged (Fig. 2f), demonstrating good resistance to ionic interference. Under the influence of starch, CGA, VC, BBR, and CNC, the maximum fluorescence intensity remains essentially unchanged (Fig. 2f), demonstrating good resistance to interference from these organic compounds.

### 3.2. Characterizations of QDs

The structural characterization of QDs was performed using TEM to verify their nanostructure. TEM images revealed well-dispersed spherical nanoparticles with an average diameter of 2.0 ± 0.3 nm, showing clear lattice fringes with a measured spacing of 0.2815 nm (Fig. 2i).

The XRD pattern (Fig. 3C) shows distinct and sharp diffraction peaks, indicating that the quantum dots have a crystalline structure. The peaks observed at approximately 30°, 40°, and 50° correspond to specific crystal planes, demonstrating the orderliness of the crystal structure. The sharpness of these peaks indicates that quantum dots have a large crystallite size and good crystallinity. In addition, there are no broad peaks in the spectrum, indicating that the amorphous components of the sample are very small, and the observed diffraction peaks correspond to the typical crystal planes of quantum dot materials. Combined with TEM results, further evidence confirms that they are nanocrystals. In order to gain a deeper understanding of the surface properties of quantum dots and explore their chemical composition, XPS was used to analyze the full XPS spectrum of quantum dots and high-resolution spectra of various elements. According to the full spectrum results (Fig. 3e), the XPS spectrum shows distinct peaks for C 1s, O 1s, and Zn 2p. In the high-resolution Zn 2p spectrum (Fig. 3f), a strong peak appears at approximately 1020 eV, indicating the presence of zinc and confirming the zinc-based nature of the quantum dots; the sharpness and intensity of the Zn 2p peak further indicate good crystallinity. In the C 1s spectrum (Fig. 3i), the strong peak observed at 284.8 eV is associated with $sp^2$-hybridized C-C/C=C bonds, indicating the possible presence of carbon-carbon double bonds. In addition, a peak observed at 288.19 eV is attributed to the C=O bond, indicating that the quantum dot surface may contain carbonyl groups. In the XPS spectrum of O 1s (Fig. 3h), a distinct peak appeared around 532 eV, which is usually related to the oxygen in oxides. For quantum dots, the O 1s peak is generally associated with surface oxide layers (ZnO) or surface functionalized groups (-OH or -COOH). In the XPS spectrum of N 1s (Fig. 3g), the peak of 400.2 eV is attributed to the N-H bond, indicating the possible presence of amino groups ($-NH_2$) on the surface of quantum dots. FTIR spectroscopy analysis identified characteristic surface functional groups: a broad absorption band at 3440 $cm^{-1}$ corresponding to O-H/N-H stretching vibrations; a distinct peak at 3196 $cm^{-1}$ indicating N-H stretching vibrations, suggesting coexisting nitrogenous groups; and the paired bands at 1584 $cm^{-1}$ ($\nu_a$-$COO^-$) and 1398 $cm^{-1}$ ($\nu$-$COO^-$) with $\Delta\nu$ = 186 $cm^{-1}$ consistent with the presence of citrate ligands (Fig. 2g). Optical properties were investigated through UV-vis absorption and fluorescence spectroscopy. The UV-vis spectrum exhibited a strong absorption peak at 247 nm (Fig. 2i). Under 360 nm excitation, the QDs showed intense fluorescence emission centered at 450 nm (Fig. 2h). Significantly, Fig. 2j directly demonstrates concentration-dependent fluorescence quenching, where incremental addition of quercetin (from low to high concentration gradient) results in progressive emission reduction, implying dynamic interactions between QDs and quercetin molecules. We conducted an in-depth investigation into the mechanism of quercetin-induced fluorescence quenching of quantum dots based on experimental results.

10.57647/jnsc.2026.1604.16

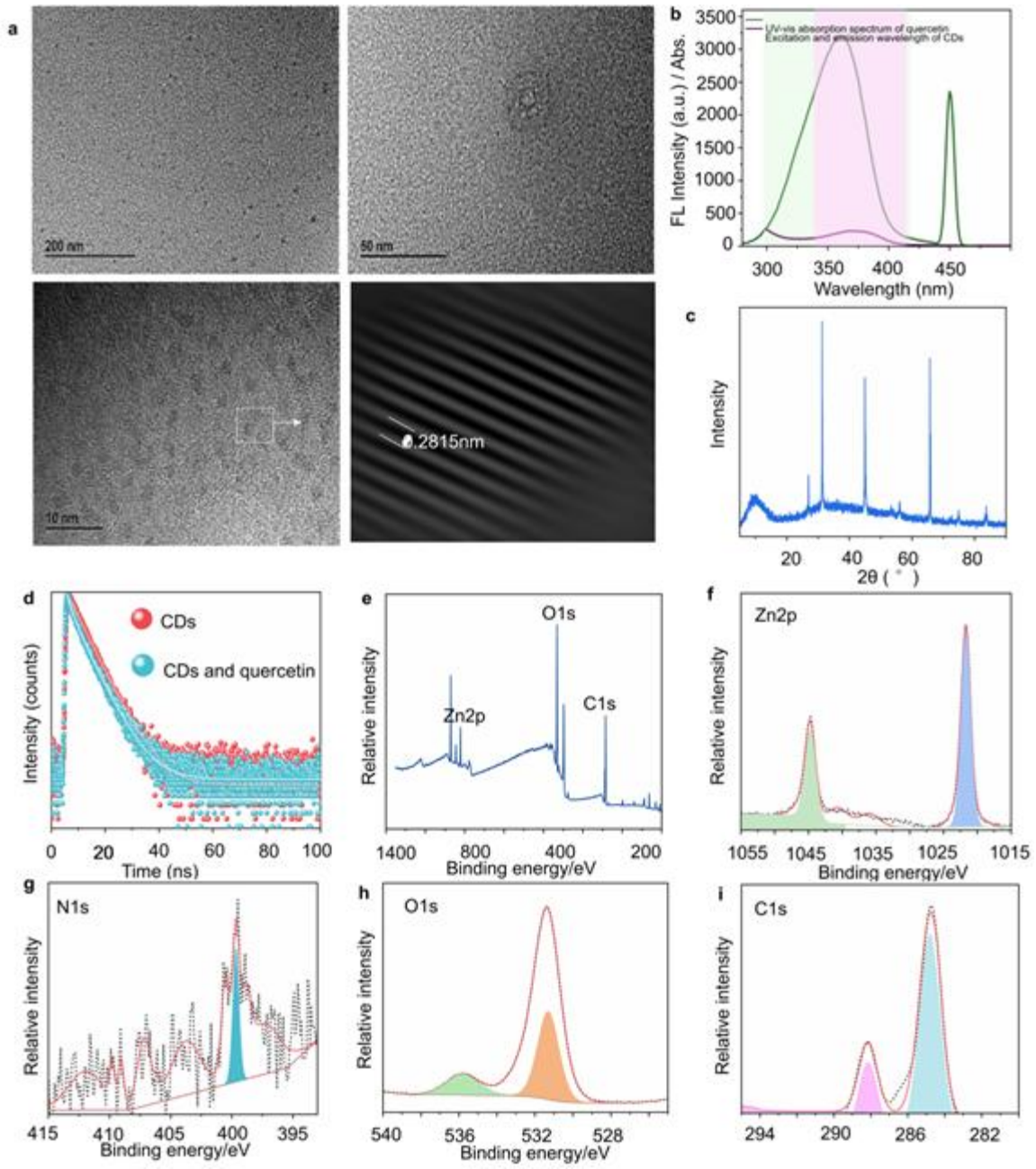


**Figure 3.** Characterization of zinc-based QDs. (a) TEM images at 200, 50 and 10 nm scales. (b) Excitation wavelength and emission wavelength of quantum dots, UV-vis absorption spectrum of quercetin. (c) XRD patterns of QDs. (d) Fluorescence lifetime spectra of quantum dots before and after the addition of quercetin. (e) XPS full spectrum of QDs. (f) Zn2p XPS. (g) N1s XPS. (h) O1s XPS. (i) N1s XPS

The excitation spectrum of the quantum dots significantly overlaps with the UV absorption band of quercetin (Fig. 3b), providing clues for two potential initial processes: the inner filter effect (IFE) and fluorescence resonance energy transfer (FRET). The inner filter effect arises from the competitive absorption of incident light by quercetin at the excitation wavelength, which directly reduces the effective excitation intensity of the quantum dots, resulting in a decrease in the apparent fluorescence intensity. However, as a "shielding" effect, IFE itself does not alter the intrinsic optical properties of the fluorophore, particularly its fluorescence lifetime. According to Fig. 3d, the fluorescence lifetime of the quantum dots was significantly shortened from 6.25 ns to 4.08 ns, ruling out static adsorption and IFE as the sole quenching mechanisms. This confirms the existence of a true intermolecular interaction leading to non-radiative deactivation of the excited-state quantum dots. Therefore, these analysis results are highly consistent with the experimental data, supporting FRET effect as the dominant quenching mechanism. Furthermore, zinc (Zn) plays a crucial and active role in the fluorescence characteristics and energy transfer processes of the quantum dots. Zn is not a passive component but an integral part of the quantum dot's electronic structure. XRD and XPS analyses confirm that Zn is predominantly incorporated within the quantum dot lattice in the $Zn^{2+}$ oxidation state. This zinc-based inorganic core defines the semiconductor properties of the quantum dots, including their energy band structure.

10.57647/jnsc.2026.1604.16

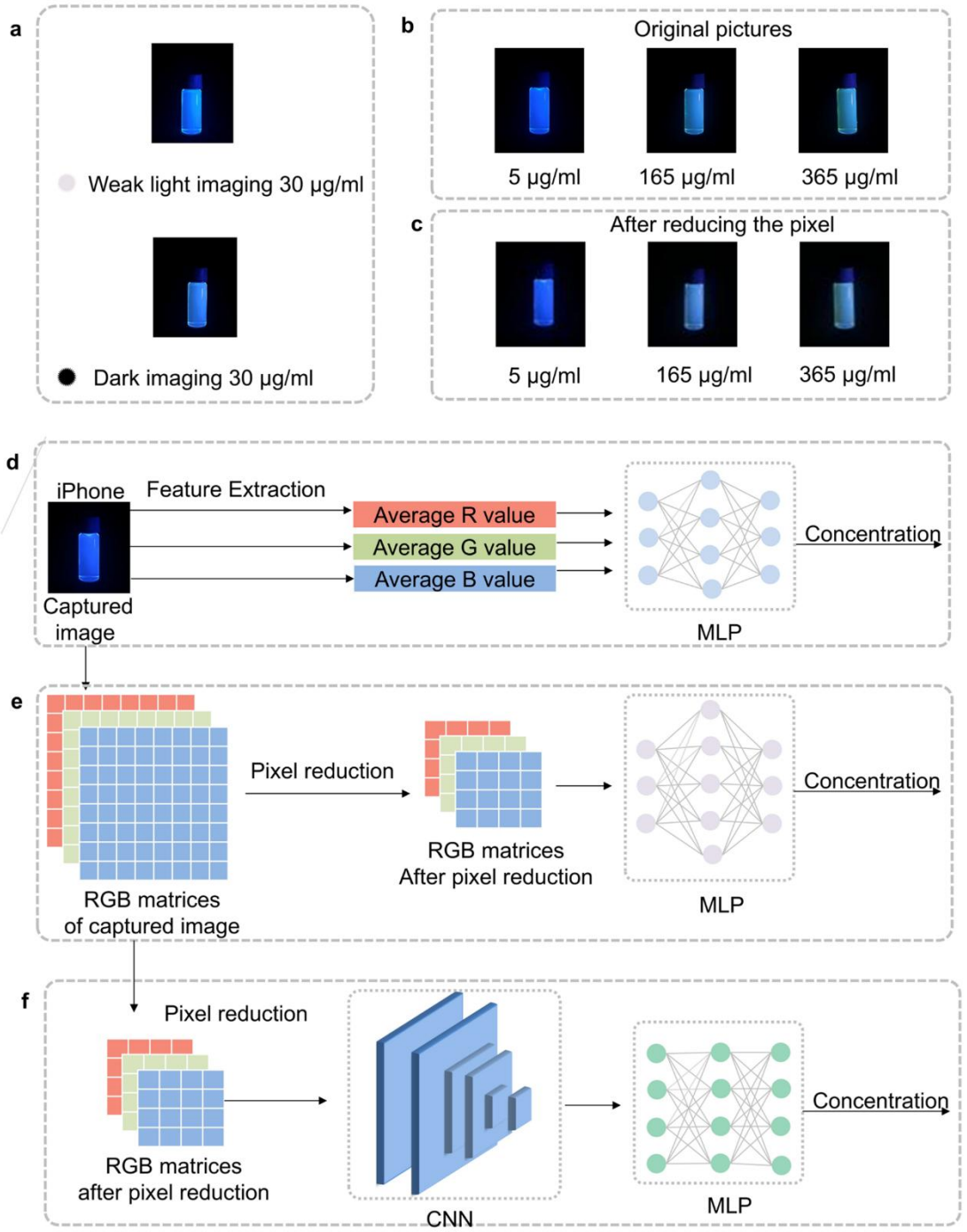


**Figure 4.** Neural network architectures for quercetin concentration prediction. (a) Comparative fluorescence imaging under dark vs. low-light conditions. (b, c) Visual comparison of image resolution before and after pixel reduction. (d) Model 1: MLP with averaged RGB input. (e) Model 2: MLP with downsampled RGB matrix. (f) Model 3: CNN-MLP hybrid with downsampled input

Specifically, both the absorption edge in the UV-Vis spectrum and the emission peak at 450 nm in the photoluminescence (PL) spectrum are attributed to electron transitions involving Zn-related energy levels.

### 3.3. Construction of machine learning models for Quercetin Detection

Quercetin standard solutions with a concentration gradient (5–500 μg/mL) were prepared for training/test sets. Since light variations in training data could degrade model accuracy during both training and testing phases, all experimental procedures were strictly conducted under controlled darkroom conditions with fixed 365 nm UV illumination (1.2 mW/cm²), ensuring lighting consistency across all acquired images (Fig. 4a). This standardization protocol minimized ambient light interference, thereby optimizing the model's ability to extract concentration-dependent features without bias from lighting artifacts. A comparison of different shooting methods was conducted to finalize the image acquisition protocol for training/test sets (Fig. S3).

The distribution map of quercetin concentration in the training and test sets is shown in Fig. S4, utilizing a total

10.57647/jnsc.2026.1604.16

of 100 concentration points, with 70% randomly selected as the training set and the remaining 30% serving as the test set.

The distribution map of quercetin concentration in training and test sets is shown in Fig. S4, based on 100 concentration points (70% for training, 30% for testing). After obtaining the images, we attempted to quantify concentration via a fluorescence intensity standard curve (Fig. S5a). When the linear range was 5-110 ug/mL, the linearity was good ($R^2 = 0.9824$, Fig. S5 c), but when the linear range was expanded to 5-500 ug/mL, the linearity was low ($R^2 = 0.7826$, Fig. S5 b), indicating that quantifying concentration through fluorescence intensity standard curve is suitable for a narrow linear range and not suitable for a wider concentration range in this experiment. Subsequently, we developed machine learning models to detect quercetin concentration. Given that CNNs are particularly adept at extracting deep-level features from images, we selected CNN to construct our concentration detection model (Model 3, Fig. 4f). Additionally, to evaluate the performance differences between CNN and commonly used ANNs, we developed two concentration measurement models based on ANN (Model 1, Fig. 4d and Model 2, Fig. 3e).

Prediction Method 1 utilized the Python programming language and the TensorFlow deep learning framework to establish a quantitative relationship between average RGB values and concentration using a Multi-Layer Perceptron (MLP) architecture. The implementation involved extracting average RGB values as input features and fluorescence concentrations as regression targets from both training and test datasets. To normalize feature scales, both the input features and target variables underwent MinMaxScaler preprocessing. The neural network architecture consisted of three fully connected (Dense) hidden layers with 64, 128, and 64 neurons, respectively, each employing ReLU activation functions, and incorporated Dropout layers between every two dense layers to mitigate overfitting. A single-neuron linear activation output layer was used to perform the regression prediction. The model configuration adopted mean squared error (MSE) as the loss function, utilized the Adam optimizer for parameter updates, and implemented mean absolute error (MAE) as the primary evaluation metric (Fig. 4d). This comprehensive implementation achieved effective concentration prediction while maintaining computational efficiency through systematic regularization strategies.

Prediction Method 2 established a regression model between image RGB matrices and concentrations using an MLP implemented in Python/TensorFlow. The methodology encompassed several critical preprocessing steps to ensure data consistency and model compatibility. All training and test images were standardized to 150 × 150 pixels resolution through the PIL library and converted to RGB format, subsequently loaded as three-dimensional arrays (150, 150, 3) into memory. Prior to model training, pixel values underwent normalization to the [0, 1] range and were flattened into one-dimensional vectors to meet MLP input requirements (Fig. 4b, c). The neural architecture incorporated three fully-connected hidden layers with 512, 256, and 128 neurons respectively, each utilizing ReLU activation functions. To enhance model generalization, Dropout layers were strategically positioned between the first two dense layers. The output layer consisted of a single neuron with linear activation for continuous concentration prediction. The model was configured with MSE as the loss function and employed the Adam optimization algorithm during training. Model performance was primarily assessed using MAE as the evaluation metric (Fig. 4e). Through the systematic implementation of dimensional reduction and regularization techniques, this approach achieved robust concentration prediction capabilities. The comprehensive architecture design effectively balanced model complexity with predictive performance while mitigating overfitting risks.

Prediction Method 3 established a regression model that correlates image RGB matrices with concentrations using a CNN implemented in Python with the TensorFlow framework. The initial feature extraction process adhered to the same protocol as Prediction Method 2. The CNN architecture consisted of three convolutional layers (Conv2D) with 32, 64, and 128 filters, respectively, all utilizing 3 × 3 kernels and ReLU activation functions. Max-pooling layers (MaxPooling2D) were integrated between each pair of convolutional layers to facilitate dimensionality reduction and mitigate overfitting. The outputs from the convolutional layers were flattened using a Flatten layer before being input into a fully connected layer comprising 64 neurons with ReLU activation. The final output layer contained a single neuron with linear activation for regression prediction. The model was trained using mean squared error (MSE) as the loss function with the Adam optimizer, while mean absolute error (MAE) served as the primary evaluation metric (Fig. 4f).

The model described above was developed using photos collected with an iPhone 14. To assess the applicability of this established model to images captured with different smartphones, Prediction Method 4 employed a Huawei P30 for photo collection, while maintaining the same processes as those used in Prediction Method 3 (Fig. S6).

### 3.4. The detection performance of quercetin

The detection error of each model was shown in Fig. 4 e and Fig. S 7. For model 1, the detection error of data points on the test set ranged from 2 to 418 μg/mL.

10.57647/jnsc.2026.1604.16

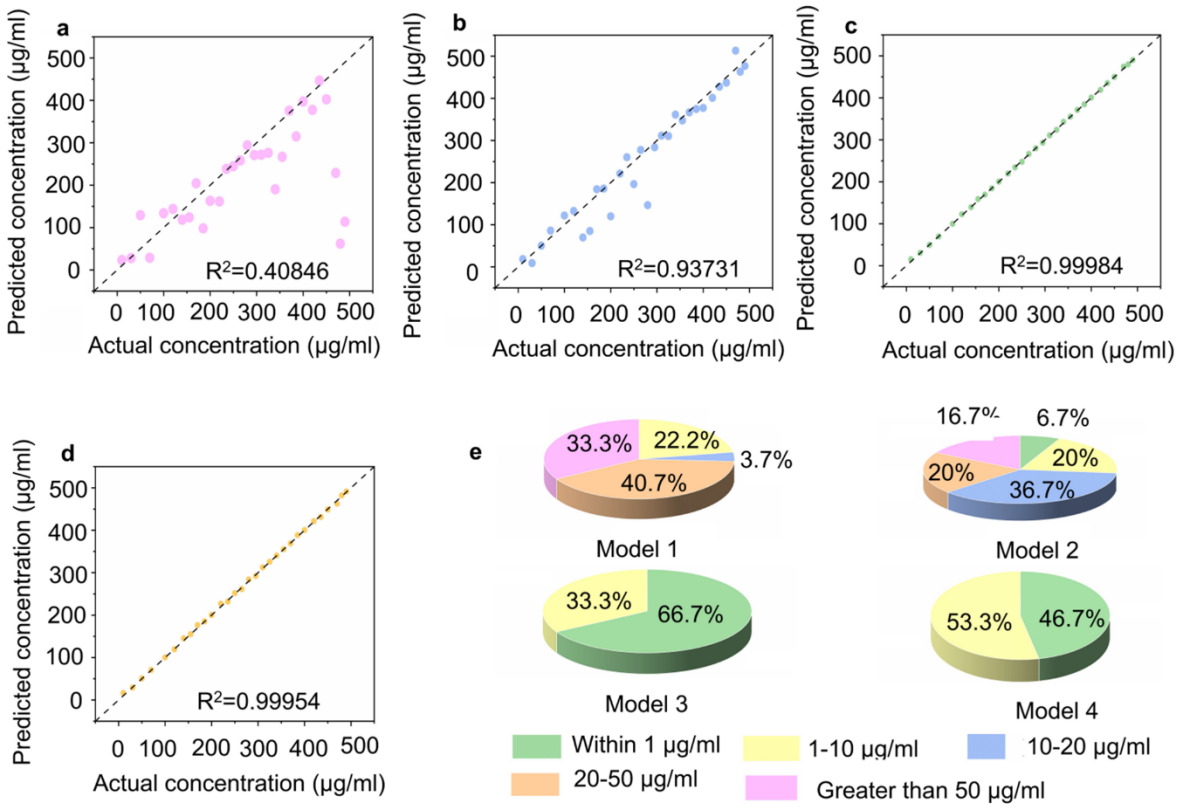


**Figure 5.** The plot of true quercetin concentration versus predicted quercetin concentration of each model. (a) Detection model 1. (b) Detection model 2. (c) Detection model 3. (d) Detection model 4. (e) Error analysis of detection models

Among these, 20% of data points exhibited detection error within 2-10 μg/mL, 10% fell within 10-20 μg/mL, and the majority (70%) showed detection errors ranging from 20-418 μg/mL, indicating exceptionally poor detection accuracy (Fig. 5a).

Model 2 demonstrated improved detection accuracy compared to Model 1. The detection error ranged from 0.3 to 134 μg/mL. Here, 26.7% of samples had detection error within 0.3-10 μg/mL, 36.7% within 10-20 μg/mL, 20% within 20-50 μg/mL, and 16.6% within 50-134 μg/mL. However, 36.7% of data points still exhibited detection errors exceeding 20 μg/mL, with some as high as 134 μg/mL (Fig. 5b). After ruling out feature extraction as the primary limitation, we concluded that the neural network model in Model 2 failed to adequately capture the intrinsic relationship between image features and concentration, leading to suboptimal accuracy.

Model 3 demonstrates superior detection accuracy with errors ranging from 0.1 to 0.54 μg/mL. Remarkably, 100% of samples exhibited detection errors within 0.1-0.54 μg/mL (Fig. 5c), representing significant improvement over both Model 1 and Model 2. The error range of Model 4 ranged from 0.05 to 7.3 μg/mL（Fig. 5d）. The key difference between Model 4 and Model 3 lies in the smartphone used for image capture. The results indicate that while Model 4 outperforms Models 1 and 2 and approaches the predictive capability of Model 3, the latter remains more accurate overall. The performance differences among the models can be explained by the following reasons. Model 1 utilized a neural network model trained on mean RGB values derived from original photographs. Although fluorescence intensity decreased with concentration in the training set images, RGB averaging substantially diminished the discriminative features. The resulting averaged RGB values exhibited minimal numerical variation, with most images approaching black-level intensities (Table S1).

This indicates that when averaging small fluorescent regions with large dark areas, critical concentration-dependent features were obscured. Consequently, the model failed to establish meaningful concentration-image relationships. As shown in Fig. S7a, the training error did not decrease with increasing training iterations, ultimately resulting in exceptionally poor detection accuracy.

Model 2 used the RGB matrices of the downsampled image as input to the model, minimizing computational load while maximizing the retention of image information (Fig. 4b, c). The influence of the black background on measurements was effectively suppressed. Consequently, the training error decreased significantly with increasing training iterations (Fig. S7b). The detection performance was markedly improved compared to Model 1. However, owing to the fully connected nature of neural networks, this architecture required an extremely large amount of training data and was prone to overfitting, resulting in still unsatisfactory detection results.

10.57647/jnsc.2026.1604.16

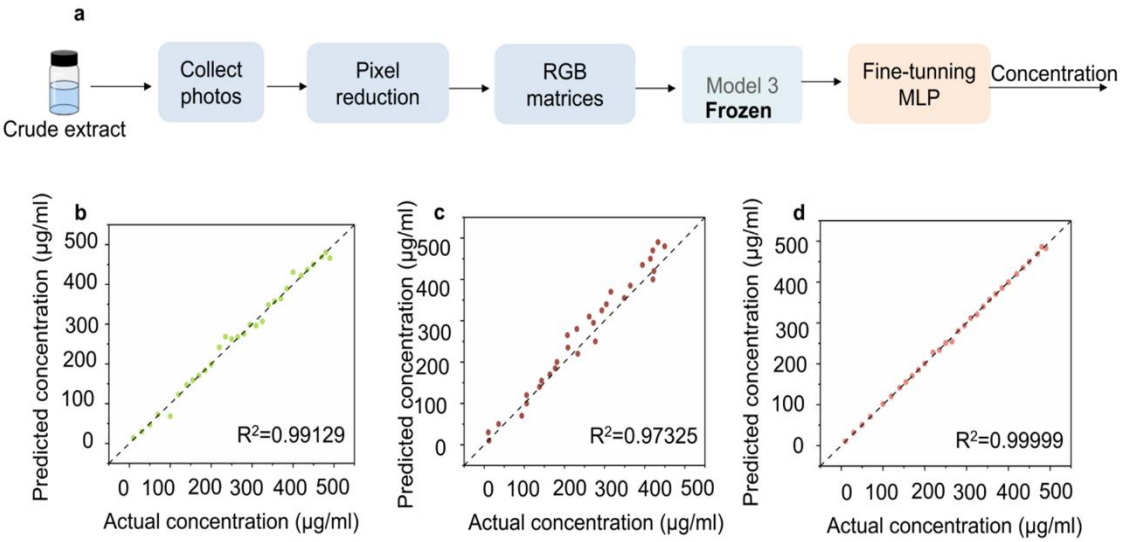


**Figure 6.** Comparative workflows for flavonoid quantification using Model 3-based architectures and the plot of total flavonoid concentration in *E. humifusa* versus predicted total flavonoid concentration of each model. (a) Model 7: Transfer learning protocol (Model 3 pre-training + MLP fine-tuning, n=10 training / n=30 test). In addition, we compared Model 7 with Models 5 and 6, Model 5: Full training set protocol (Model 3 retrain, n=70 training / n=30 test). Model 6: Reduced training set protocol (Model3 retrain, n=10 training / n=30 test). (b) Detection model 5. (c) Detection model 6. (d). Detection model 7

Enhanced performance in Method 3 was achieved through two key innovations: the utilization of RGB matrices that preserve fluorescence characteristics without the dilution of features caused by dark backgrounds, and the implementation of a CNN architecture capable of effectively learning complex relationships between image features and concentration profiles. The hierarchical feature extraction mechanism of the CNN enabled accurate concentration predictions by simultaneously capturing localized fluorescence patterns and global image attributes, thus overcoming the limitations inherent in prior approaches. As evidenced in Fig. S7c, the training error of Model 3 converged to smaller values at an accelerated rate. These advancements establish a clinically transferable framework for photo-based concentration quantification with diagnostic-grade precision.

### 3.5. Determination of total flavonoids in *E. humifusa*

A total of 5-500 μg/mL of total flavonoid extract from *E. humifusa* was prepared to obtain the training and test sets (Fig. S4). To verify the applicability of the quercetin prediction model for total flavonoid determination in *E. humifusa* extract, Model 5 adopted Model 3's training protocol (70 concentration points as training set, 30 as test set). Results indicated that 73.3% of data points had detection errors of 0.04-10 μg/mL, while 26.7% ranged from 10-34 μg/mL (Fig. 6b), demonstrating robust predictive accuracy. However, the extensive training data requirement hindered practical deployment. To facilitate field detection, we developed Model 6 using ten concentration points (5, 15, 25, 35, 45, 55, 65, 75, 85, and 95 μg/mL) as the training set with Model 3's methodology. Results showed: 23.3% errors at 2-10 μg/mL, 50% at 10-40 μg/mL, and 26.7% at 40-58 μg/mL (Fig. 6c). While less accurate than Model 5, this method offered greater practicality for field applications. To optimize both convenience and accuracy, Model 7 (Fig. 6a, d) utilized Model 6's datasets but incorporated Model 3's pre-training with an added fully connected neural network for fine-tuning, thereby adapting the quercetin prediction method for total flavonoid quantification. Results demonstrated that 100% data points with errors of 0.1-10 μg/mL, achieving superior accuracy compared to Models 5-6 while maintaining operational simplicity. The recovery rate of spiked quercetin in the actual sample reached 81.04% -102.92%, with RSD values ranging from 1.17% to 3.07% (Table S2).

### 3.6. Comparison with other detection methods

According to literature studies [9, 25-33], the detection method established in this study demonstrates an ultra-wide linear range (5–500 μg/mL), significantly outperforming most comparative literature, and allows for the direct detection of high-concentration or highly variable samples without dilution. This provides unique practical advantages in rapid screening and process monitoring.

Although the recovery rate (81.04%–102.92%) is within an acceptable range, the lower limit is slightly lower and the range is wider, indicating that there is room for improvement in the method's accuracy and stability. Overall, this method is positioned as a practical technique for routine analysis. While it is less sensitive than high-precision fluorescence or electrochemical methods, its broad detection range makes it suitable for quality control in pharmaceutical raw materials, food, and traditional Chinese medicine materials. (Table 1).

10.57647/jnsc.2026.1604.16

**Table 1.** Comparison between the proposed method and other methods

| Methods | Limit of Detection (LOD) (μg/mL) | Limit of Quantification (LOQ) (μg/mL) | Linear Range (μg/mL) | Spike Recovery |
|---|---|---|---|---|
| HPLC | 0.00488 | 0.03906 | 0.03906 – 200 | 99.589%-103.060% |
| HPLC | 0.12 | 0.35 | 0.45 – 57.60 | 96.9% – 103.1% |
| HPLC | 25 | / | 25 – 150 | 97.50% – 103.30% |
| Electrochemistry | 0.0011 | / | 0.0018 – 3.0224 | / |
| Electrochemistry | 0.000535 | / | 0.00151 – 0.15112 | 98.20% – 102.42% |
| Fluorescence detection | 0.053 | / | 1.0 – 12.5 | / |
| Fluorescence detection | 0.006 | / | 0 – 15.112 | 94.2% – 96.1% |
| Fluorescence detection | 0.0042 | / | 0.0302 – 13.6 | 92.6% – 105% |
| Capillary electrophoresis | 0.0062 | 0.0124 | 2.1 – 33.3 | 93.21% |
| UV | 4.99 | 16.46 | 0 – 18.15 | / |
| This paper | / | / | 5-500 | 81.04% -102.92% |

For total flavonoid content determination, our experiment demonstrated a linear range of 5–500 μg/mL, whereas prior studies [34-38] reported 8.16–300 μg/mL. This represents a 1.6-fold reduction in the lower detection limit and a 1.6-fold expansion of the upper limit (Fig. S9).

## 4. Conclusion

This study monitored the changes in the fluorescence intensity of QDs in the presence of varying quercetin concentrations. A quantitative relationship between the quercetin concentration and image features extracted from smartphone-captured photographs was established using a convolutional neural network (CNN). The model was successfully applied to determine the total flavonoid content in real samples, expressed as quercetin equivalents, demonstrating its potential as a rapid quantitative approach. Although promising, the universal applicability of this method for total flavonoid determination in different plant species or matrices requires further rigorous validation. For instance, quantitative results may be biased if a sample contains flavonoids with quenching efficiencies significantly different from those of quercetin. While the efficacy of this method has been validated for *Euphorbia humifusa*, its application to other plant species warrants further exploration. This work presents a novel strategy that integrates QDs, smartphone imaging, and CNN to rapidly determine quercetin concentration within three minutes based on simple image input. The method offers significant advantages in cost, speed, simplicity, and accuracy. However, reproducible measurement requires careful control of imaging conditions, as variables such as the operator, environment, and camera device may influence the results. Future work will focus on standardizing these parameters to enhance the method's robustness and practical applicability.

10.57647/jnsc.2026.1604.16

## Acknowledgments

This work was supported by the National Natural Science Foundation of China (No. 32371536 and 32271527).

**Conflict of Interest**
The authors declare that they have no known competing financial interests or personal relationships that could have appeared to influence the work reported in this paper.

**Ethical Approval**
This study does not involve human participants or living organisms, and no ethical approval was required.

**Data Availability**
Data will be made available on request.

## Reference

[1] Ma, X.X., Li, N., Wang, R.F., Ma, J.X., Zhu, N.H., Li, T.T., Zhang, Z.X., Li, H.F., Wang, S.L., Zhang, H.H.: Nondestructive detection of total flavonoids content in daylily using Vis-NIR and NIR hyperspectral imaging: data fusion combined with SHAP for model interpretability. Chemom. Intell. Lab. Syst. **268,** 105575 (2026)

[2] Zhang, L.S., Yu, L.L., Yang, S.C., Yang, X.F., Ye, S.D., Ma, H.W., Hu, J.Y., Liu, Y., Duan, Z.J., Wen, X.D.: Natural Deep Eutectic Solvent-Based Ultrasonic-Assisted Simultaneous Extraction of Phenolic Acids and Flavonoids from Erigeron breviscapus and Its Extraction Mechanism Analysis. ACS Sustain. Chem. Eng. **14**, 249-259 (2026)

[3] Xu, C., Li, J.B., Liu, J., Ma, Y.X., Wang, X.S., Xie, Y.F., Chen, C.X., Ji, W.: Rapid construction of interfacial plasmonic nanoarray for SERS sensing of flavonoids. Biosens. Bioelectron. **271**, 117044 (2025)

[4] Sullam, E.M., Adam, K.M., Liu, J.J., Chen, H.L., Xiao, J.X.: Silicon quantum dots-based fluorescent sensor for the detection of cobalt with high sensitivity and selectivity. Chin. Chem. Lett. **35**, 108476 (2024)

[5] Qin, Y.L., Zhong, X.Y., Liang, C.H., Liang, Z.W., Nong, Y.Y., Deng, L.J., Guo, Y., Li, J.F., Zhang, M.L., Tang, S.Q., Wei, L.Y.,

Yang, Y., Liang, Y.H., Wu, J.X., Lam, Y.M., Su, Z.H.: Nanozyme-based colorimetric sensor arrays coupling with smartphone for discrimination and "segmentation-extraction-regression" deep learning assisted quantification of flavonoids. Biosens. Bioelectron. **263**, 116604 (2024)

[6] Gupta, P., Tamrakar, G., Biswas, S., Dhundhe, R.S., Soni, V.K., Das, H.S., Sahu, P., Chaturwedi, A.K., Kashyap, K.N., Akitsu, T., Hait, M.: Quantum Dots as a Fluorescent Sensor for Detecting Heavy Metal Ions in Aqueous Environment: An Overview. ES Chem. Sustain. **1**, 1359 (2024)

[7] Somathube, S., Daramola, O.A., Lokole, P.B., Safari, J.B., Siwe-Noundou, X., Dejene, F.B.: Synthesis of ZnSe QDs: Effects of stabilizer on the optical properties and structural morphology. Results Phys. **73**, 108262 (2025)

[8] Zhou, J., Xiao, Y., Huang, J.Q., Huang, M.L., Zhang, S., Li, K.: A novel molecular imprinted probe with hybrid ratio fluorescent for visual detection of imazapyr. Microchem. J. **198**, 110116 (2024)

[9] Kadian, S., Manik, G.: Sulfur doped graphene quantum dots as a potential sensitive fluorescent probe for the detection of quercetin. Food Chem. **317**, 126457 (2020)

[10] El-Shafie, A.S., Osman, A.I., Al-Hashimi, N., Al-Saad, K., Al-Ghouti, M.A., Ibrahim, Y., Shibl, M.F., El-Azazy, M.: Valorization of olive pruning lignocellulosic residues into carbon dots: A sustainable approach for discrimination of Iron species. Int. J. Biol. Macromol. **318**, 144628 (2025)

[11] Borwornmote, S., Suksuratin, P., Rodpai, R., Sukeepaisarnjaroen, W., Intapan, P.M., Maleewong, W., Chuchuen, O.: Optical Diagnosis of Liver Cirrhosis and Hepatocellular Carcinoma using Machine Learning-Assisted Serum Raman Spectroscopy. Eng. Sci. **36**, 1667 (2025)

[12] Ed-Dahmouny, A., Zeiri, N., Arraoui, R., Baser, P., Es-Sbai, N., Sali, A., Murshed, M.N., Duque, C.A.: Machine learning prediction of electric field-dependent absorption coefficient in CdTe/CdS quantum dots. Mater. Today Phys. **58**, 101851 (2025)

[13] Cherni, A., Zeiri, N., Hayrapetyan, D.B., Ed-Dahmouny, A., El Sayed, M.E., Samir, A., Duque, C.A.: Machine learning models for predicting the hydrogenic impurity nonlinear optical rectification in GaAs/AlGaAs Tetrapod core/shell quantum dots under the effect of temperature. Mater. Today Phys. **58**, 101833 (2025)

[14] Wu, X.Y., Yan, H.Y., Cao, Y., Yuan, Y.: Prediction acrylamide contents in fried dough twist based on the application of artificial neural network. Food Chem.: X. **24**, 102007 (2024)

[15] Chen, Y.Y.. Li, S.P., Zhang, X.B., Gao, X.X., Jiang, Y.H., Wang, J.B., Jia, X.Y., Ban, Z.J.: Prediction of apple moisture content based on hyperspectral imaging combined with neural network modeling. Sci. Hortic. **338**, 113739 (2024)

[16] Li, Y.G., Dong, Y.X., Wang, R.J., Lin, Z.H., Lin, J.J., Ji, X.Y., Ye, B.C.: Biomimetic Electrochemical Sensor Based on Single-Atom Nickel Laccase Nanoenzyme for Quercetin Detection. Anal. Chem. **96**, 2610-2619 (2024)

[17] Yuan, W.D., Zhou, H.P., Zhang, C., Zhou, Y., Wu, Y., Jiang, X.S., Jiang, H.Z.: Determination and visualization of moisture content in *Camellia oleifera* seeds rapidly based on hyperspectral imaging combined with deep learning. Spectrochim. Acta, Part A: Mol. Biomol. Spectrosc. **330**, 125676 (2025)

[18] Ficzere, M., Meszaros, L.A., Diószegi, A., Banrevi, Z., Farkas, A., Lenk, S., Galata, D.L., Nagy, Z.K.: UV imaging for the rapid at-line content determination of different colourless APIs in their tablets with artificial neural networks. Int. J. Pharm. **657**, 124174 (2024)

[19] Gomes, V., Fernandes, A., Martins-Lopes, P., Pereira, L., Faia, A.M., Melo-Pinto, P.: Characterization of neural network generalization in the determination of pH and anthocyanin content of wine grape in new vintages and varieties. Food Chem. **218**, 40-46 (2017)

[20] Tian, R., Calderon, A.D., Liu, X., Fu, H.: Discovery of Quaternary Perovskites via Stacked Machine Learning and Generative Models. Eng. Sci. **35**, 1561 (2025)

[21] Tang, A.H., Yang, G.J., Li, Z.H., Pan, Y.C., Liu, Y., Long, H.L., Chen, W.N., Zhang, J., Yang, Y., Yang, X.D., Xu, B.: Estimation of SOC using VNIR and MIR hyperspectral data based on spectral-to-image transforming and multi-channel CNN. Comput. Electron. Agric. **231**, 109986 (2025)

[22] Huang, Q., Yu, H.Y., Jiang, Z.H., Xie, Y.F., Pan, D., Gui, W.H.: Multi-component quantitative analysis of LIBS using adaptively optimized multi-branch CNN. Opt. Laser Technol. **179**, 111282 (2024)

[23] Yuan, Q., Wang, J.J., Zheng, M.W., Wang, X.L.: Multi-component quantitative analysis of LIBS using adaptively optimized multi-branch CNN. Constr. Build. Mater. **350**, 128799 (2022)

[24] Li, J.B., Luo, J.N., Tian, Q.J., Yang, S.H., Bu, Y.H., Chi, Q., Guo, W.C.: Transfer of apple soluble solids content prediction model across cultivars based on domain-adversarial neural network. Postharvest Biol. Technol. **225**, 113494 (2025)

[25] Patil, N., Mahajan, H.: Development and Validation of RP-HPLC Method for Simultaneous Qualitative and Quantitative Estimation of Curcumin and Quercetin in Bulk Mixture. Indian J. Pharm. Educ. **56**, 247–254 (2022)

[26] Careri, M., Corradini, C., Elviri, L., Nicoletti, I., Zagnoni, I.: Direct HPLC Analysis of Quercetin and trans-Resveratrol in Red Wine, Grape, and Winemaking Byproducts. J. Agric. Food Chem. **51**, 5226–5231 (2003)

[27] Arvand, M., Anvari, M.: A graphene-based electrochemical sensor for sensitive detection of quercetin in foods. J. Iran. Chem. Soc. **10**, 841–849 (2013)

[28] Dou, L.W., Han, H., Yang, B.B., Lin, C.X., Pan, S.B., Li, Q. J., Yan, P.Z., Zhao, D.S., Chang, X.B., Li, J.: Rapid determination of quercetin and caffeic acid in honeysuckle tea by high efficiency electrochemical sensor. J. Food Meas. Charact. **17**, 5821–5827 (2023)

[29] Zuo, P.L., Xiao, D.L., Gao, M.M., Peng, J., Pan, R.F., Xia, Y., He, H.: Single-step preparation of fluorescent carbon nanoparticles, and their application as a fluorometric probe for quercetin. Microchim. Acta. **181**, 1309–1316 (2014)

[30] Gao, R., Wang, L., Yang, Y., Ni, J., Zhao, L., Dong, S., Guo, M.: Simultaneous determination of oleanolic acid, ursolic acid, quercetin and apigenin in Swertia mussotii Franch by capillary zone electrophoresis with running buffer modifier. Biomed. Chromatogr. **29**, 402–409 (2015)

[31] Liu, H.P., Shi, X.F., Zhang, Y.C., Li, Z.X., Zhang, L., Wang, Z.Y.: Quantitative Analysis of Quercetin in Euphorbia helioscopia L by RP-HPLC. Cell Biochem. Biophys. **61**, 59–64 (2011)

[32] Duhan, J., Bisht, A., Kumar, H., Obrai, S.: Graphitic nitride co-doped with sodium and sulphur as fluorescent and UV-Vis probe for quercetin detection. Surf. Interf. **52**, 104927 (2024)

[33] Jiang, W.J., He, R., Zhang, F., Wang, L., Wei, Y.L.: Water-soluble sulfur quantum dots as a potential sensitive fluorescent probe for quercetin detection and cell imaging. Food Chem. **464**, 141618 (2025)

[34] Sheng, Z.L., Wan, P.F., Dong, C.L., Li, Y.H.: Optimization of total

flavonoids content extracted from *Flos Populi* using response surface methodology. Ind. Crop. Prod. **43**, 778–786 (2013)

[35] Ardekani, M.R.S., Hajimahmoodi, M., Oveisi, M.R., Sadeghi, N., Jannat, B., Ranjbar, A.M., Gholam, N., Moridi, T.: Comparative Antioxidant Activity and Total Flavonoid Content of Persian Pomegranate (*Punica granatum* L.) Cultivars. Iran. J. Pharm. Res. **10**, 519–524 (2011)

[36] Qin, P.Y., Wang, Q., Shan, F., Hou, Z.H., Ren, G.X.: Nutritional composition and flavonoids content of flour from different buckwheat cultivars. Int. J. Food Sci. Technol. **45**, 951–958 (2010)

[37] Wang, J., Zhou, N.D., Zhu, Z.Q., Huang, J.Y., Li, G.X.: Detection of flavonoids and assay for their antioxidant activity based on enlargement of gold nanoparticles. Anal. Bioanal. Chem. **388**, 1199–1205 (2007)

[38] Li, Y.M., Zhang, Q., Fang, Q., Zhu, H., Zong, X.L., Gao, X., Shi, Y., Qin, K.M.: A novel ultrasound-assisted enzyme extraction method of total flavonoids from Viticis Fructus and processed Viticis Fructus: Comparison of in vitro antioxidant activity. Ultrason. Sonochem. **110**, 107045 (2024)

10.57647/jnsc.2026.1604.16